

# A peculiar hard X-ray counterpart of a Galactic fast radio burst

A. Ridnaia<sup>1</sup>, D. Svinkin<sup>1</sup>, D. Frederiks<sup>1</sup>, A. Bykov<sup>1</sup>, S. Popov<sup>2,3</sup>, R. Aptekar<sup>1</sup>,  
S. Golenetskii<sup>1</sup>, A. Lysenko<sup>1</sup>, A. Tsvetkova<sup>1</sup>, M. Ulanov<sup>1</sup>, and T. Cline<sup>4</sup>

<sup>1</sup>Ioffe Institute, 26 Politekhnicheskaya, St Petersburg, 194021, Russia

<sup>2</sup>Sternberg Astronomical Institute, Lomonosov Moscow State University, Moscow, 119234, Russia

<sup>3</sup>Higher School of Economics, Department of Physics, Moscow, 101000, Russia

<sup>4</sup>NASA Goddard Space Flight Center, Greenbelt, Maryland, USA (retired)

## ABSTRACT

Fast radio bursts are bright, millisecond-scale radio flashes of yet unknown physical origin<sup>1</sup>. Recently, their extragalactic nature has been demonstrated<sup>2,3</sup>, and an increasing number of the sources have been found to repeat<sup>4</sup>. Young, highly magnetized, isolated neutron stars - magnetars - have been suggested as the most promising candidates for fast radio burst progenitors owing to their energetics and high X-ray flaring activity<sup>5,6</sup>. Here we report the detection with the *Konus-Wind* detector of a hard X-ray event of April 28, 2020, temporarily coincident with a bright, two-peak radio burst<sup>7,8</sup> with properties remarkably similar to those of fast radio bursts. The source of the radio burst is located<sup>7</sup> in the direction to the Galactic magnetar SGR 1935+2154, which recently entered an active state. We show that a separation between two peaks of the double-peaked X-ray burst is nearly the same as that of the radio peaks, confirming that the X-ray and radio emission most likely have a common origin. Thus, this is the first simultaneous detection of a fast radio burst from a Galactic magnetar and its high-energy counterpart. The total energy emitted in X-rays in this burst is typical of bright short magnetar bursts, but its spiky light curve and an unusual hardness of the energy spectrum distinguish the April 28 event among multiple 'ordinary' flares detected from SGR 1935+2154 previously. This, and a recent non-detection<sup>9</sup> of radio emission from two typical bright soft bursts<sup>10</sup> from the same magnetar, may imply the existence of a special class of magnetar flares capable of producing fast radio bursts.

## MAIN TEXT

Magnetars<sup>11,12</sup> are rare, young, isolated neutron stars with strong magnetic field<sup>13</sup> ( $B \sim 10^{14} - 10^{15}$  G). Soft Gamma-ray Repeaters (SGRs), discovered in 1979<sup>14,15</sup> through the detection of repeating short bursts in the hard X-ray/soft  $\gamma$ -ray range, were later associated with the magnetar activities<sup>16</sup>. During an active phase, which may last from several days to a year or more, and is followed by a long quiescent period, SGRs sporadically emit short (fraction of a second) bursts of hard X-rays, with photon energies below a hundred keV and implied peak X-ray luminosities of  $L_X \sim 10^{38} - 10^{42}$  erg/s. Only a dozen burst-emitting magnetars are known so far<sup>17</sup> and, up to now, no counterpart to such bursts is identified at other wavelengths.

SGR 1935+2154 is a new member of the magnetar family, discovered on 2014 July 5 through a series of short bursts<sup>18,19</sup>. Extensive follow-up observations carried out during the first eight months since the source discovery with *Swift*/X-ray Telescope, *Chandra* and *XMM-Newton* X-ray observatories confirmed that SGR 1935+2154 was indeed a magnetar with a spin period  $P \sim 3.24$  s and  $\dot{P} = 1.43 \times 10^{-11}$  s s<sup>-1</sup>, implying a surface dipole magnetic field value of  $B \sim 2.2 \times 10^{14}$  G well within the typical range of magnetars<sup>20</sup>. The source position lies very close to the geometric center of the Galactic supernova remnant (SNR) G57.2+0.8<sup>21</sup>, whose distance estimates range from 6.6 kpc<sup>22</sup> up to 12.5 kpc<sup>23</sup>. Accounting for the uncertainty in distance, we adopt 10 kpc in this paper. Since its discovery SGR 1935+2154 has been one of the most burst-prolific magnetars. During the recent activation, started in April 2020, it exhibited multiple bright, short X-ray bursts, culminating, on April 27, in a burst ‘forest’ made up of rapid sequences of multiple flares during which the count rate never returns to baseline<sup>24-26</sup>.

The next day, at  $\approx 14:34:33$  UT ( $T_{\text{CHIME}}$ ), a bright, millisecond-scale radio burst from the direction of SGR 1935+2154 was detected by CHIME/FRB backend<sup>7</sup> in the 400-800 MHz band, and, independently, by STARE2<sup>8</sup> in the 1.4 GHz band. The CHIME/FRB light curve had a two-peak structure with two components  $\sim 5$  ms wide separated by  $\sim 30$  ms. A preliminary inferred fluence of this burst, which properties are remarkably similar to those of fast radio bursts (FRBs), was estimated to a few kJy-ms by CHIME/FRB, and to  $>1.5$  MJy-ms by STARE2. Simultaneously, the hard X-ray burst was observed with INTEGRAL<sup>27,28</sup>, AGILE<sup>29</sup>, *Konus-Wind*<sup>30</sup> (KW), and *Insight-HXMT*<sup>31</sup>. The burst triggered KW at  $T_0 =$

14:34:24.447 UT (geocentric time, see Methods). The KW light curve (Fig. 1) shows a gradually rising, double-peaked pulse, which starts at  $\sim T_0 - 0.220$  s, peaks at  $\sim T_0 - 0.020$  s and  $\sim T_0 + 0.008$  s, and decays to background level at  $\sim T_0 + 0.264$  s. Although the precise time of the radio burst arrival has not been reported by the observers at the time of writing this paper, the KW  $T_0$  is consistent with the de-dispersed time  $T_{\text{CHIME}}$  at infinite frequency within  $\sim 60$  ms. The separation between the two main peaks in the KW light curve ( $\sim 30$  ms) appears nearly the same as that of the radio peaks reported by CHIME. Thus, we conclude that the KW event and the radio burst originate from the same source and we witness the first simultaneous detection of an FRB-like burst from a Galactic magnetar and its hard X-ray counterpart.

The photon energies measured by KW during this event extend to beyond 250 keV. Our spectral analysis (Methods) shows, that the energy spectrum in the 20–500 keV band is well described by two spectral models: an exponentially-cutoff power law function (CPL) and a sum of two blackbody functions (2BB). For the time-averaged spectrum (from  $T_0$  to  $T_0 + 0.256$  s), the CPL low-energy photon index  $\alpha$  is  $-0.72^{+0.47}_{-0.46}$  and the peak energy in  $\nu F_\nu$  spectrum  $E_p$  is  $85^{+15}_{-10}$  keV (all spectral parameter errors are given at the 90% confidence level). To examine the possible presence of a hard power-law component, we fit this spectrum by a joint smoothly broken power-law function (the Band GRB function, see Methods). The fit with this model results in nearly the same low-energy photon index and  $E_p$ , with only an upper limit on the high-energy photon index ( $\beta < -2.7$ ). From the fit with two blackbody functions, the cold and hot blackbody temperatures are estimated to  $11^{+3}_{-4}$  keV and  $31^{+12}_{-7}$  keV, respectively.

Derived from our analysis, the photon index  $\alpha$  has relatively wide confidential intervals extending to the values about -1.5 (Extended Data Fig. 2). While the indices of  $\alpha \leq -1$  are less likely from the KW observations, they do allow to speculate about a single power law spectrum of the event extending from the radio to hard X-rays (Fig. 2). Although the lower limits on the burst radio flux estimated from the inferred radio fluences exceed the extrapolation of the best-fit CPL model ( $\alpha \simeq -0.7$ ) by more than 6 orders of magnitude, the inferred flux in the 400-800 MHz band ( $\gtrsim 25$  Jy) appears to be consistent with a broadband CPL spectrum with  $\alpha \sim -1.35$ , which is within the 95% confidence bound of the best-fit spectral model. To explain properties of simultaneous radio and X/ $\gamma$ -ray bursts from SGR 1935+2134 it is tempting to use approaches developed for FRBs, as magnetar scenarios for these extragalactic transients seem to be the most reliable, now. Data obtained with KW and other instruments allows interpretation in

the framework of magnetar models of FRBs and opens exciting prospects for its validation (see Emission scenarios section in Methods).

The burst total energy fluence, measured in the 20–500 keV band over the total duration of 0.484 s, is  $(9.7 \pm 1.1) \times 10^{-7}$  erg/cm<sup>2</sup>, and the peak energy flux is  $(7.5 \pm 1.0) \times 10^{-6}$  erg/cm<sup>2</sup>/s, in a 16 ms time interval corresponding to the second peak in the light curve. For the source distance 10 kpc we estimate the burst total energy release in X-rays to  $\approx 1.2 \times 10^{40}$  erg and the peak isotropic X-ray luminosity to  $L_X \approx 0.9 \times 10^{41}$  erg/s, both typical of bright, short magnetar flares. From the inferred lower limits on the radio fluence<sup>7,8</sup>, the radio luminosity  $L_r$  is  $\sim (10^{33} - 10^{36})$  erg/s, and the ratio of radio to high energy luminosity  $L_r/L_X$  estimates to  $\sim (10^{-8} - 10^{-5})$ .

We note, that the implied  $L_r/L_X$  in the April 28 flare is of the same order, as in the case of FRBs, if we relate them to magnetar giant (and hyper) flares<sup>14,32,33</sup> with  $L_X \sim (10^{44} - 10^{47})$  erg/s, as radio luminosities of FRBs are estimated to be in the range  $L_r \sim (10^{38} - 10^{42})$  erg/s<sup>1</sup>. In future, with more detections of coincident radio and X-ray bursts, the proximity of Galactic magnetars would allow to distinguish between different proposed scenarios of emission, and compare it with the data on FRBs. At the moment, it is pre-mature to claim that the detected flare from SGR 1935+2154 is a real twin of FRBs, as energy scales of these two types of events are different by several orders of magnitude. Unfortunately, with existing all-sky gamma- and X-ray monitors even hyperflares of magnetars hardly can be detected from distances  $>100$  Mpc<sup>34</sup>. May be, a more realistic approach can be related to radio observations of nearby galaxies at distances  $\lesssim$  few Mpc, as in this case flares like the one from SGR 1935+2154 can produce radio flux of  $\sim$  few mJy. Note, that FRB-like radio transients already have been detected from the Andromeda galaxy (M31)<sup>35</sup>, and also there are known candidates for magnetar giant flares from M31<sup>36</sup> and two other galaxies nearby<sup>37–39</sup>.

As concluding remarks, we would like to emphasize two important peculiarities of the April 28 X-ray burst. First, its slowly rising, spiky light curve is quite unusual for magnetars bursts, which typically demonstrate smooth time profiles starting with a prominent, sharp rise of the intensity (see Extended Data Fig. 3). Second, while the implied shape of the burst hard X-ray spectrum is in line with other magnetar bursts, the emission in this event extends up to a few times higher energies than typical ( $\gtrsim 250$  keV vs.  $\lesssim 100$  keV) and, accordingly, the derived  $E_p$  is the highest among all the bursts observed from

SGR 1935+2154 so far<sup>40-42</sup>, including the highly-energetic,  $\sim 1.7$  s long intermediate flare<sup>41</sup> (Fig. 3). This, and recent non-detection<sup>9</sup> of radio emission from two typical bright soft bursts<sup>10</sup> from the same magnetar, may imply the existence of a special class of magnetar flares capable of producing FRB-like bursts.

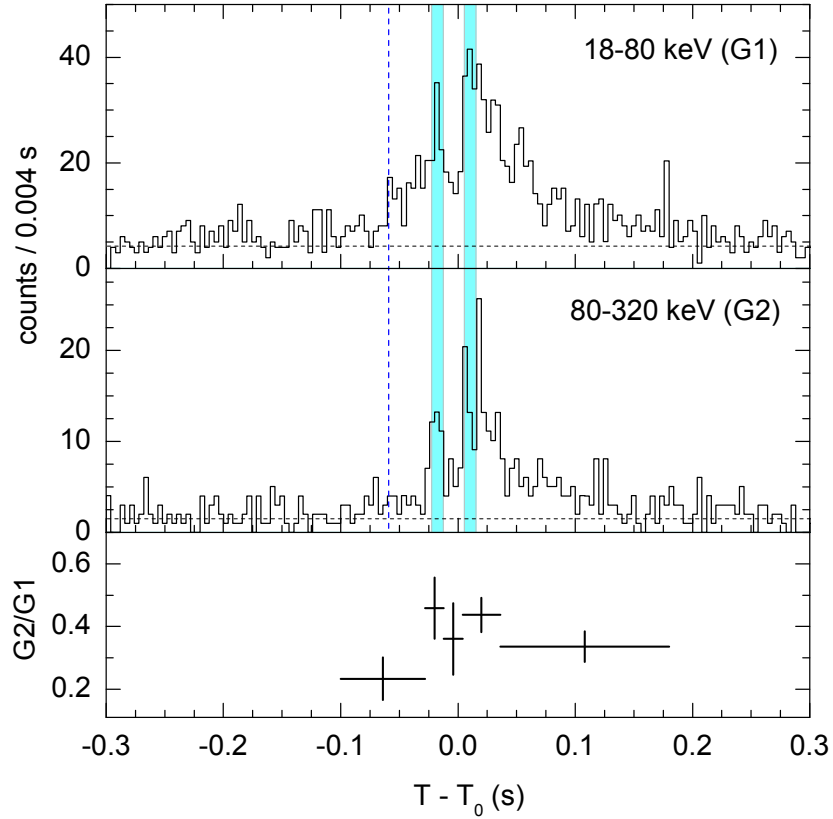


**Figure 1.** Hard X-ray burst from SGR 1935+2154 of April 28, 2020. The burst time history is shown, as recorded by *Konus-Wind* in two energy bands: G1 (18-80 keV, top panel) and G2 (80-320 keV, middle panel). Background count rates are shown with horizontal dashed lines. In the course of the burst, the emission hardness, illustrated by the evolution of the hardness ratio  $G2/G1$  (bottom panel) exhibits no pronounced variation, with a hint of the positive hardness-intensity correlation near main peaks.  $T_0$  corresponds to 14:34:24.447 UT (geocentric time). The vertical dashed line corresponds to the radio burst time reported by CHIME/FRB<sup>7</sup>, as corrected for the dispersion delay and converted to the Earth center (details are given in Methods). Two time intervals, shown by shaded bars, represent the temporal structure of the two-peak radio burst<sup>7</sup>. As the precise time of the radio burst arrival has not been reported, the position of the first interval is chosen arbitrarily to match first peak of the double-peaked X-ray burst, and the second interval is 30 ms apart. The separation between the two main peaks in the *Konus-Wind* light curve is nearly the same as that of the radio peaks.

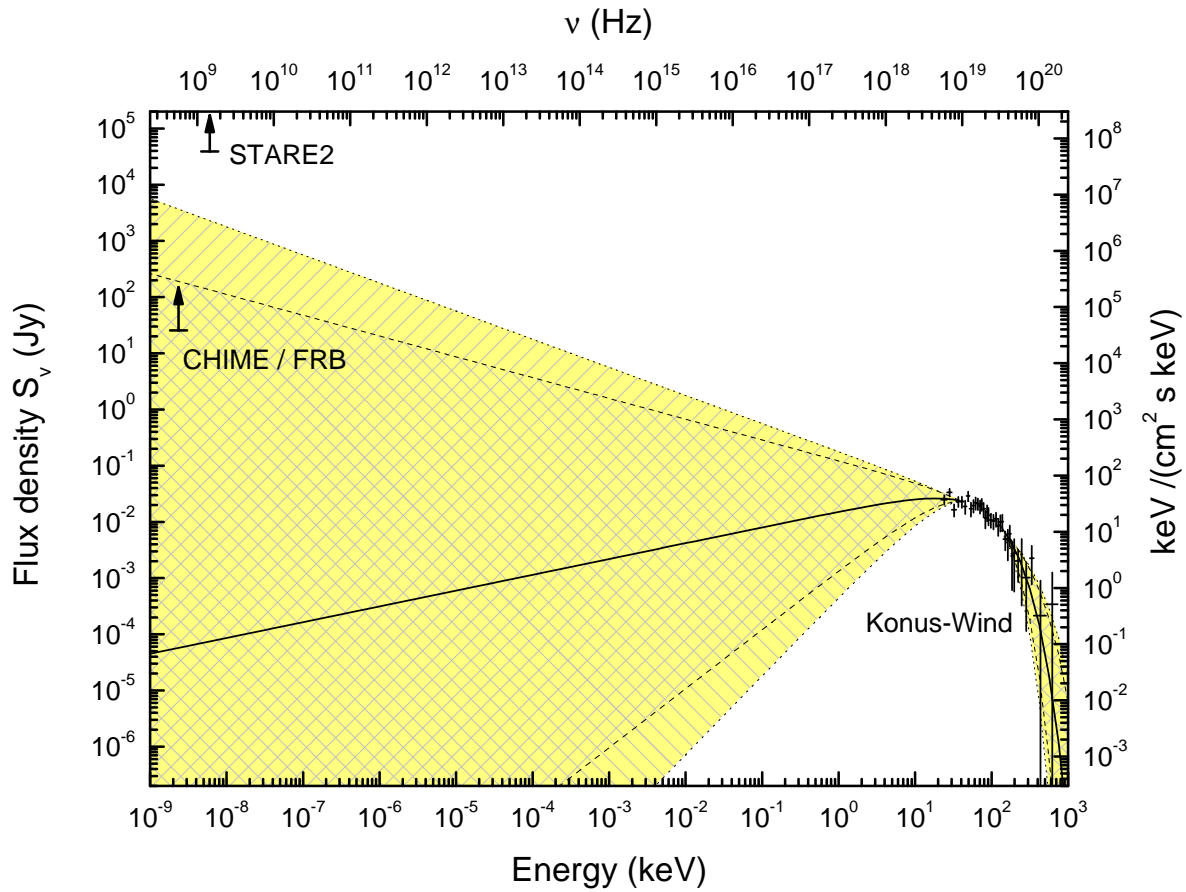


**Figure 2.** Radio to X-ray spectral energy distribution. The high-energy data points are from *Konus-Wind*. The solid line is the best-fit to the KW data with CPL function, dashed and dotted lines correspond to the boundaries of CPL parameter posterior distribution at 95% and 99.7% integrated probability, respectively. The lower limits on 400-800 MHz and 1.4 MHz radio fluxes are derived from the inferred burst fluences reported by CHIME<sup>7</sup> and STARE2<sup>8</sup>, respectively. Although the 400-800 MHz flux density exceeds the extrapolation of the best-fit CPL model ( $\alpha=-0.72$ ) by 6 orders of magnitude, this flux is consistent with a broadband CPL spectrum with  $\alpha \sim -1.35$ , within the 95% confidence bound. Details of the KW spectral analysis are given in Methods and also in Extended Data Figures 1 and 2.

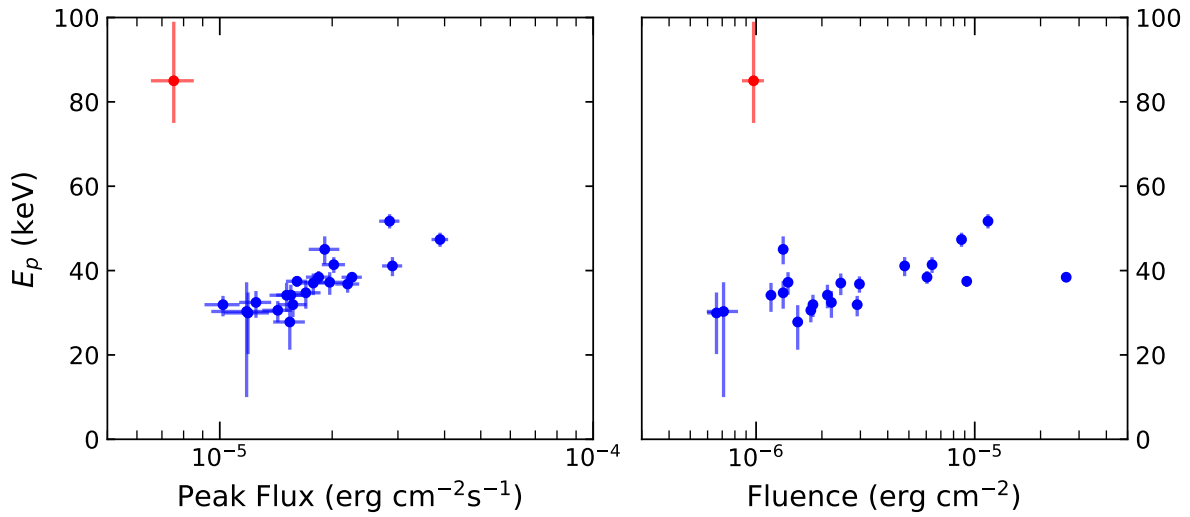


**Figure 3.** Peak energy fluxes, fluences, and peak energies of SGR 1935+2154 bursts. Left panel:  $E_p$  (the peak energy of  $\nu F_\nu$  spectrum) vs. peak energy flux in the 20–500 keV range. Right panel: energy fluence (in the same range) vs.  $E_p$ . Twenty short X-ray bursts detected by *Konus-Wind* in 2015–2020 are shown by blue symbols and the red point represents the April 28 burst. Unlike other bursts, the observed emission in this event extends up to  $\gtrsim 250$  keV and, accordingly,  $E_p$  is the highest among all the bursts observed from SGR 1935+2154 so far. The error bars are given at the 90% confidence level.

## References

1. Cordes, J. M. & Chatterjee, S. Fast Radio Bursts: An Extragalactic Enigma. *ARA&A* **57**, 417–465 (2019). [1906.05878](#).
2. Ravi, V. *et al.* A fast radio burst localized to a massive galaxy. *Nature* **572**, 352–354 (2019).
3. Marcote, B. *et al.* A repeating fast radio burst source localized to a nearby spiral galaxy. *Nature* **577**, 190–194 (2020). [2001.02222](#).
4. CHIME/FRB Collaboration CHIME/FRB Discovery of Eight New Repeating Fast Radio Burst Sources. *Astrophys. J.* **885**, L24 (2019). [1908.03507](#).
5. Popov, S. B. & Postnov, K. A. Hyperflares of SGRs as an engine for millisecond extragalactic radio bursts. *Evolution of Cosmic Objects through their Physical Activity*, 129–132 (2010). [0710.2006](#).
6. Beloborodov, A. M. A Flaring Magnetar in FRB 121102?. *Astrophys. J.* **843**, L26 (2017). [1702.08644](#).
7. Scholz, P. A bright millisecond-timescale radio burst from the direction of the Galactic magnetar SGR 1935+2154. *The Astronomer's Telegram, No. 13681, #1 (2020)* **13681** (2020).
8. Bochenek, C. *et al.* Independent detection of the radio burst reported in ATel #13681 with STARE2. *The Astronomer's Telegram, No. 13684, #1 (2020)* **13684** (2020).
9. Kirsten, F. *et al.* Simultaneous multi-frequency limits on radio emission at the time of a bright X-ray burst from SGR 1935+215. *The Astronomer's Telegram, No. 13735, #1 (2020)* **13735** (2020).
10. Ridnaia, A. *et al.* Konus-Wind observation of SGR 1935+2154 activity on 2020 May 10. *GRB Coordinates Network, Circular Service, No. 27715, #1 (2020)* **27715** (2020).
11. Mereghetti, S., Pons, J. & Melatos, A., Magnetars: Properties, Origin and Evolution. *Space Sci. Rev.* **191**, 315–338 (2015). [1503.06313](#).
12. Kaspi, V. M. & Beloborodov, A. M. Magnetars. *ARA&A* **55**, 261–301 (2017). [1703.00068](#).
13. Duncan, R. C. & Thompson, C. Formation of Very Strongly Magnetized Neutron Stars: Implications for Gamma-Ray Bursts. *Astrophys. J.* **392**, L9 (1992).

14. Mazets, E. P., Golentskii, S. V., Ilinskii, V. N., Aptekar, R. L. & Guryan, Iu. A. Observations of a flaring X-ray pulsar in Dorado. *Nature* **282**, 587–589 (1979).
15. Mazets, E. P., Golentskii, S. V. & Guryan, Y. A. Soft gamma-ray bursts from the source B1900+14. *Soviet Astronomy Letters* **5**, 343 (1979).
16. Kouveliotou, C. *et al.* An X-ray pulsar with a superstrong magnetic field in the soft  $\gamma$ -ray repeater SGR1806 - 20. *Nature* **393**, 235–237 (1998).
17. Olausen, S. A. & Kaspi, V. M. The McGill Magnetar Catalog. *Astrophys. J. Supp.* **212**, 22 (2014). [1309.4167](#).
18. Stamatikos, M., Malesani, D., Page, K. L. & Sakamoto, T. GRB 140705A: Swift detection of a short burst. *GRB Coordinates Network, Circular Service, No. 16520, #1 (2014)* **16520** (2014).
19. Lien, A. Y. *et al.* GRB 140705A: Swift-BAT refined analysis of a possible newly discovered SGR 1935+2154. *GRB Coordinates Network, Circular Service, No. 16522, #1 (2014)* **16522** (2014).
20. Israel, G. L. *et al.* The discovery, monitoring and environment of SGR J1935+2154. *Mon. Not. R. Astron. Soc.* **457**, 3448–3456 (2016). [arXiv:astro-ph/1601.00347](#).
21. Gaensler, B. M. GRB 140705A / SGR 1935+2154: Probable association with supernova remnant G57.2+0.8. *GRB Coordinates Network, Circular Service, No. 16533, #1 (2014)* **16533** (2014).
22. Zhou, P. *et al.* Revisiting the distance, environment and supernova properties of SNR G57.2+0.8 that hosts SGR 1935+2154. *arXiv e-prints*, arXiv:2005.03517 (2020). [2005.03517](#).
23. Kothes, R., Sun, X., Gaensler, B. & Reich, W. A Radio Continuum and Polarization Study of SNR G57.2+0.8 Associated with Magnetar SGR 1935+2154. *Astrophys. J.* **852**, 54 (2018). [1711.11146](#).
24. Ricciarini, S *et al.* high bursting activity of SGR 1935+2154: CGBM observations. *GRB Coordinates Network, Circular Service, No. 27663, #1 (2020)* **27663** (2020).
25. Palmer, D. M. A Forest of Bursts from SGR 1935+2154. *GRB Coordinates Network, Circular Service, No. 27665, #1 (2020)* **27665** (2020).
26. Ridnaia, A *et al.* Konus-Wind observation of a very intense bursting activity of SGR 1935+2154. *GRB Coordinates Network, Circular Service, No. 27667, #1 (2020)* **27667** (2020).

27. Mereghetti, S. *et al.* INTEGRAL IBIS and SPI-ACS detection of a hard X-ray counterpart of the radio burst from SGR 1935+2154. *The Astronomer's Telegram*, No. 13685, #1 (2020) **13685** (2020).
28. Mereghetti, S. *et al.* INTEGRAL discovery of a burst with associated radio emission from the magnetar SGR 1935+2154. *arXiv e-prints*, arXiv:2005.06335 (2020). [2005.06335](#).
29. Tavani, M. *et al.* AGILE detection of a hard X-ray burst in temporal coincidence with a radio burst from SGR 1935+2154. *The Astronomer's Telegram*, No. 13686, #1 (2020) **13686** (2020).
30. Ridnaia, A *et al.* Konus-Wind observation of hard X-ray counterpart of the radio burst from SGR 1935+2154. *GRB Coordinates Network, Circular Service*, No. 27669, #1 (2020) **27669** (2020).
31. Zhang, S.-N. *et al.* Insight-HXMT detection of a bright short x-ray counterpart of the Fast Radio Burst from SGR 1935+2154. *The Astronomer's Telegram*, No. 13687, #1 (2020) **13687** (2020).
32. Hurley, K. *et al.* An exceptionally bright flare from SGR 1806-20 and the origins of short-duration  $\gamma$ -ray bursts. *Nature* **434**, 1098–1103 (2005).
33. Frederiks, D. D. *et al.* Giant flare in SGR 1806-20 and its Compton reflection from the Moon. *Astronomy Letters* **33**, 1–18 (2007). [astro-ph/0612289](#).
34. Svinkin, D. S., Hurley, K., Aptekar, R. L., Golenetskii, S. V. & Frederiks, D. D. A search for giant flares from soft gamma-ray repeaters in nearby galaxies in the Konus-WIND short burst sample. *Mon. Not. R. Astron. Soc.* **447**, 1028–1032 (2015). [1411.5589](#).
35. Rubio-Herrera, E., Stappers, B. W., Hessels, J. W. T. & Braun, R. A search for giant flares from soft gamma-ray repeaters in nearby galaxies in the Konus-WIND short burst sample. *Mon. Not. R. Astron. Soc.* **428**, 2857–2873 (2013). [1210.4660](#).
36. Mazets, E. P. *et al.* A Giant Flare from a Soft Gamma Repeater in the Andromeda Galaxy (M31). *Astrophys. J.* **680**, 545–549 (2008). [0712.1502](#).
37. Frederiks, D. D. *et al.* On the possibility of identifying the short hard burst GRB 051103 with a giant flare from a soft gamma repeater in the M81 group of galaxies. *Astronomy Letters* **33**, 19–24 (2007). [astro-ph/0609544](#).

38. Svinkin, D. *et al.* Improved IPN error box for GRB 200415A (consistent with the Sculptor Galaxy). *GRB Coordinates Network, Circular Service, No. 27595, #1 (2020)* **27595** (2020).
39. Frederiks, D. *et al.* Konus-Wind observation of GRB 200415A (a magnetar Giant Flare in Sculptor Galaxy?). *GRB Coordinates Network, Circular Service, No. 27596, #1 (2020)* **27596** (2020).
40. Lin, L. *et al.* Burst Properties of the Most Recurring Transient Magnetar SGR J1935+2154. *Astrophys. J.* **893**, 156 (2020). [2003.10582](#).
41. Kozlova, A. V. *et al.* The first observation of an intermediate flare from SGR 1935+2154. *Mon. Not. R. Astron. Soc.* **460**, 2008–2014 (2016). [1605.02993](#).
42. Ridnaia, A. *et al.* Konus-Wind observation of a bright burst from SGR 1935+2154. *GRB Coordinates Network, Circular Service, No. 27631, #1 (2020)* **27631** (2020).

## Methods

### Observations

**Konus-Wind** Konus-Wind<sup>43</sup> (KW) consists of two identical NaI(Tl) scintillation detectors, each with  $2\pi$  sr field of view, mounted on opposite faces of the rotationally stabilized *Wind* spacecraft<sup>44</sup>, such that one detector (S1) points towards the south ecliptic pole, thereby observing the south ecliptic hemisphere, while the other (S2) observes the north ecliptic hemisphere. The April 28, 2020 burst from SGR 1935+2154 triggered detector S2, the incident angle was  $47^\circ$ .

Each KW detector is 5 inches in diameter and 3 inches in height, placed into an aluminum container faced with a beryllium entrance window. The crystal scintillator is viewed by a photomultiplier tube through a 20 mm thick lead glass, which provides effective detector shielding from the spacecraft's background in the soft spectral range. The detector effective area is  $\sim 80$ – $160$  cm<sup>2</sup>, depending on the photon energy and incident angle. The energy range of gamma-ray measurements covers the incident photon energy interval from 20 keV up to 16 MeV.

The instrument has two operational modes: waiting and triggered. While in the waiting mode, the count rates (lightcurve) are recorded in three energy band G1 (18–80 keV), G2 (80–320 keV), and G3 (320–1300 keV) with 2.944 s time resolution. When the count rate in G2 exceeds a  $\approx 9\sigma$  threshold above the background on one of two fixed time-scales, 1 s or 140 ms, the instrument switches into the triggered mode.

In the triggered mode, light curves are recorded in the same G1, G2, and G3 bands, starting from 0.512 s before the trigger time  $T_0$  with time resolution varying from 2 ms up to 256 ms. For the burst of interest, the whole time history is available with the 2 ms resolution.

Spectral measurements are carried out, starting from the trigger time  $T_0$  (no multichannel spectra are available before  $T_0$ ) in two overlapping energy intervals with nominal boundaries 20–1300 keV (PHA1) and 260 keV–16 MeV (PHA2) with 64 spectra being recorded for each interval over a 63-channel, pseudo-logarithmic energy scale. The first four spectra are measured with a fixed accumulation time of 64 ms in order to study short bursts and they cover about a half of the April 28 burst time history.

For the presented analysis we use a standard KW dead time (DT) correction procedure for light curves (with a DT of a few microseconds) and spectra (with a DT of  $\sim 42$  microseconds). The burst of interest has a moderate photon flux of  $\sim 10^4$  counts  $s^{-1}$ , so no additional correction, which was used, e.g., in the analysis<sup>45</sup> of the KW detection of the 1998 August 27 giant flare from SGR 1900+14, is required.

**The burst arrival times in X-ray and radio bands** The burst triggered KW on 2020-04-28 at  $T_0 = 14:34:24.084$  UTC (52464.084 seconds since midnight). The burst data became available on ground at about 2020-04-28 20:00 UTC.

The *Wind* ephemeris at  $T_0$  R.A. =  $22^\circ 502$ , Dec. =  $9^\circ 547$  (J2000), and the distance from the Earth center of 1326000.1 km were calculated using the *Wind* predicted ephemeris. The ephemeris data and their description are available at [https://spdf.gsfc.nasa.gov/pub/data/wind/orbit/pre\\_or/](https://spdf.gsfc.nasa.gov/pub/data/wind/orbit/pre_or/) and [https://cdaweb.gsfc.nasa.gov/misc/NotesW.html#WI\\_OR\\_PRE](https://cdaweb.gsfc.nasa.gov/misc/NotesW.html#WI_OR_PRE), respectively. The *Wind* clock accuracy is measured with a few day interval, the measurement closest to the burst time is available in [https://pwgdata.sci.gsfc.nasa.gov/pub/wind\\_clock/wind\\_20-119-13-21-00.cc\\_rpt](https://pwgdata.sci.gsfc.nasa.gov/pub/wind_clock/wind_20-119-13-21-00.cc_rpt). For the burst detection date the estimated clock correction was 2.7 ms (the lag of the *Wind* on-board clock), so, the corrected KW trigger time is  $T_0 = 14:34:24.087$  UTC (52464.087 s).

Using the SGR 1935 + 2154 position<sup>20</sup> R.A. =  $19^h 34^m 55.^s 5978s$ , Dec. =  $+21^\circ 53' 47'' 7864$  (J2000.0) we calculated the Earth-crossing time (the KW trigger time corrected for the *Wind*-Earth propagation time) to be  $T_{0,KW, Earth} = 14:34:24.447$  UTC (52464.447 s).

The topocentric burst arrival time at  $\nu=400$  MHz in the CHIME/FRB backend was  $T_{CHIME} \approx 14:34:33$  UTC<sup>7</sup>. Using the dispersion measure  $DM=332.8$  pc  $cm^{-3}$ , as given in the same reference, we estimated the arrival time correction for infinite frequency  $\Delta t_{disp} = 4.149 \times 10^3 (DM / (\text{pc cm}^{-3})) / (\nu / 1\text{MHz})^2 \approx 8.630$  s. We estimated propagation time delay from CHIME site to the Earth center to be  $\sim 18$  ms. Thus, the geocentric CHIME detection time at infinite frequency is  $T_{CHIME, Earth} = 14:34:24.388$  UTC which is  $\approx 60$  ms earlier than  $T_{0,KW, Earth}$  (Fig. 1).

## Data analysis

**Temporal analysis** For the temporal analysis we used time histories from  $T_0 - 0.512$  s to  $T_0 + 0.512$  s in three energy bands: G1 (18–80 keV), G2 (80–320 keV) and G3 (320–1300 keV), with a time resolution of 2 ms. The total burst duration  $T_{100}$ , and the  $T_{90}$  and  $T_{50}$  durations (the time intervals that contain 5% to 95% and 25% to 75% of the total burst count fluence, respectively<sup>46</sup>, see Extended Data Table 1), were calculated in this work using the light curves in G1 and G2 energy band. Burst start and end times in the each band were calculated at the  $5\sigma$  with a method similar to that developed for BATSE<sup>47</sup>. The background count rates, estimated using the data from  $T_0 + 8.448$  s to  $T_0 + 98.560$  s, are  $1056 \text{ s}^{-1}$  (G1),  $380 \text{ s}^{-1}$  (G2), and  $173 \text{ s}^{-1}$  (G1).

**Spectral analysis** We analyzed two energy spectra, accumulated from  $T_0$  to  $T_0 + 0.064$  s (the peak spectrum) and from  $T_0$  to  $T_0 + 0.256$  s (time-integrated spectrum), which approximately correspond to the second peak and the entire burst emission after  $T_0$ , respectively. The background spectrum was extracted from the interval  $T_0 + 8.448$  s to  $T_0 + 98.560$ .

We performed the spectral analysis in XSPEC, version 12.10.1<sup>48</sup>, using the following spectral models: a simple power law (PL), a custom exponential cutoff power-law (CPL) parametrized with peak of  $\nu F_\nu$  spectrum and energy flux as the model normalization, and the Band GRB function<sup>49</sup>. We also used single blackbody (BB) function, and a sum of two blackbody functions with the normalization proportional to the surface area (2BB), which have been shown to be the best-fits to the broadband spectra of SGR bursts<sup>50–53</sup>. The details of each model are presented below.

The power law model:

$$f_{\text{PL}} = A(E/E_n)^\alpha ; \quad (1)$$

the custom exponentially cutoff power law (CPL):

$$\begin{aligned} n(E) &= (E/E_n)^\alpha \exp(-E(2 + \alpha)/E_p) \\ f_{\text{CPL}} &= F \times n(E) / \int_{E_{\min}}^{E_{\max}} n(E) E dE ; \end{aligned}$$

the Band function:

$$f_{\text{Band}} = A \begin{cases} (E/E_n)^\alpha \exp\left(-\frac{E(2+\alpha)}{E_p}\right), & E < (\alpha - \beta) \frac{E_p}{2+\alpha} \\ (E/E_n)^\beta \left[\frac{E_p(\alpha-\beta)}{E_n(2+\alpha)}\right]^{(\alpha-\beta)} \exp(\beta - \alpha), & E \geq (\alpha - \beta) \frac{E_p}{2+\alpha}, \end{cases}$$

where  $f$  is a photon spectrum, measured in  $\text{cm}^{-2} \text{s}^{-1} \text{keV}^{-1}$ ,  $A$  is a model normalization,  $E_n = 100 \text{ keV}$  is a pivot energy,  $E_p$  is the peak energy of the  $\nu F_\nu$  spectrum, and  $F$  is the model energy flux in the  $E_{\min} - E_{\max}$  energy band;  $\alpha$  and  $\beta$  are the low-energy and high-energy photon indices, respectively. The single blackbody (BB) function and 2BB models are a single `bbbodyrad` and a sum of two `bbbodyrad` XSPEC models, respectively. The results of our spectral analysis are presented in Extended Data Tables 2 and 3.

The Poisson data with Gaussian background statistic (PG-stat) was used in the model fitting process as a figure of merit to be minimized. The spectral channels were grouped to have a minimum of one counts per channel to ensure the validity of the fit statistic.

The best-fit spectral parameters and their confidence intervals were calculated using Bayesian statistics and a Markov chain Monte Carlo (MCMC) technique. We performed MCMC simulations using the XSPEC implementation of the Goodman-Weare algorithm where an ensemble of "walkers", which are vectors of the fit parameters, "explore" the parameter space via random steps determined by the walker positions on the previous iteration. We evolved eight walkers for a total of  $4 \times 10^6$  steps, after discarding ("burn") the initial 10000 steps to ensure the chain reached a steady state. We use PG-stat likelihood and Gaussian priors centered on the initial fit result with variance matrix based on the covariance matrix of the fit. We then marginalized over the model normalization parameter to generate posterior probabilities for  $\alpha$  and  $E_p$ , using the XSPEC `margin` command. Then we find the best-fit parameters as a peak of the marginalized posterior distribution. The marginalized posterior distributions presented in Extended Data Fig. 2 in terms of integrated probability were produced directly from chain FITS files using Python3 programming language libraries Numpy<sup>54</sup> and Matplotlib<sup>55</sup>. in a way similar to the XSPEC `plot margin` command. The contours encompassing the particular probability were constructed using Matplotlib `contour` function from the integrated probability distribution.

**Burst energetics** The total energy fluence  $S$  and the peak energy flux  $F_{\text{peak}}$  of the burst were derived using the energy flux of the best-fit CPL spectral model in the 20 keV–500 keV band. Since the time-integrated spectrum accumulation interval differs from the  $T_{100}$  interval a correction which accounts for the emission outside the time-integrated spectrum was introduced when calculating  $S$ .  $F_{\text{peak}}$  was calculated on the 16 ms scale using the best-fit CPL spectral model for the spectrum near the peak count rate. To obtain  $F_{\text{peak}}$ , the model energy flux was multiplied by the ratio of the peak count rate to the average count rate in the spectral accumulation interval. The Konus-Wind spectrum presented in Fig. 2 was measured over the interval from  $T_0$  to  $T_0 + 256$  ms and the derived flux was scaled to the average count rate in the interval  $\pm 64$  ms around  $T_0$ , which covers two main peaks of the burst. Both corrections mentioned above were made using counts in the G1+G2 light curve.

## Emission scenarios

To explain properties of simultaneous radio and X/ $\gamma$ -ray bursts from SGR 1935+2134 it is tempting to use approaches developed for FRBs<sup>1</sup>, as magnetar scenarios for these extragalactic transients seem to be the most reliable, now. Magnetar models of FRBs can be divided into two broad groups based on the regions where the emission is generated. The first group of models<sup>56–58</sup> assumes emission from a relativistic outflow which interacts with the surrounding medium. Derived from our analysis, the CPL photon index  $\alpha$  has relatively wide confidential intervals extending to the values about -1.5, which are close to the indices typical for the fast cooling synchrotron regime widely discussed in GRB spectral models<sup>59–63</sup>. While the indices of  $\alpha \leq -1$  are less likely from the KW observations, they do allow to speculate about a single power law spectrum of the event extending from the radio to hard X-rays (see Fig. 2). The single power law can be expected in a relativistic outflow with internal shocks<sup>6</sup> or colliding magnetized shells<sup>64</sup> driven by the magnetospheric flares in the magnetar wind. In the later scenario the magnetic pulses produced by the magnetospheric flares of the total luminosity  $L \geq 10^{41}$  erg/s propagate beyond the light cylinder (of radius  $1.5 \times 10^{10}$  cm) with Lorentz factor  $\Gamma \sim 15$ . They can collide at the dissipation region of the internal shells at the distance  $\sim ct_{\text{var}}\Gamma^2 \sim 3.4 \times 10^{10}$  cm<sup>61</sup> i.e. just beyond the light cylinder for the flare parameters. The estimated value of magnetic field of the pulse in the dissipation region  $\sim 10^4$  G. The electron-positrons in the colliding magnetized shells can be accelerated up to the Lorentz factor  $\gamma \gtrsim 10^4$

over the time of  $10^{-5}$  s which is enough to produce the hard X-ray synchrotron photons with particle spectral indices  $\geq 1$ <sup>65,66</sup>. In an alternative scenario of magnetar transient emission<sup>67</sup>, recently applied to FRBs<sup>68</sup>, radio/X-ray flares resemble solar flares. Non-thermal particles are generated due to reconnection in a magnetar magnetosphere, i.e. below the light cylinder. Radio emission is generated early after the reconnection. If this radiation originates at a given distance from a neutron star, it is confined in a relatively narrow band, but a spread in emission distances result in a wider spectrum. X-ray emission, which mainly appears when many electron-positron pairs are produced, is expected to be thermalized. This can be compatible with the observations if thermal fit for the high energy part of the spectrum is used.

## References for Methods

### References

43. Aptekar, R. *et al.* Konus-W Gamma-Ray Burst Experiment for the GGS Wind Spacecraft. *Space Sci. Rev.* **120**, 265–272 (1995).
44. Harten, R. & Clark, K. The Design Features of the GGS Wind and Polar Spacecraft. *Space Sci. Rev.* **71**, 23–40 (1995).
45. Mazets, E. P. *et al.* Activity of the soft gamma repeater SGR 1900+14 in 1998 from Konus-Wind observations: 2. The giant August 27 outburst. *Astron. Lett.* **25**, 635–648 (1999). [arXiv: astro-ph/9905196](https://arxiv.org/abs/astro-ph/9905196).
46. Kouveliotou, C. *et al.* Identification of two classes of gamma-ray bursts. *Astrophys. J.* **413**, L101–L104 (1993).
47. Koshut, T. M. *et al.* Systematic Effects on Duration Measurements of Gamma-Ray Bursts. *Astrophys. J.* **463**, 570 (1996).
48. Arnaud, K. A. *et al.* XSPEC: The First Ten Years. *ASP Conf. Ser.* **101**, 17 (1996).
49. Band, A. J. *et al.* BATSE observations of gamma-ray burst spectra. I - Spectral diversity. *Astrophys. J.* **413**, 281–292 (1993).

50. Feroci, M. *et al.* Broadband X-Ray Spectra of Short Bursts from SGR 1900+14. *Astrophys. J.* **612**, 408–413 (2004). [arXiv:astro-ph/0405104](#).
51. Olive, J.-F. *et al.* Time-resolved X-Ray Spectral Modeling of an Intermediate Burst from SGR 1900+14 Observed by HETE-2 FREGATE and WXM. *Astrophys. J.* **616**, 1148–1158 (2004). [arXiv:astro-ph/0403162](#).
52. Lin, L. *et al.* Broadband Spectral Investigations of SGR J1550-5418 Bursts. *Astrophys. J.* **756**, 54 (2012). [arXiv:1207.1434](#).
53. van der Horst, A. J. *et al.* SGR J1550-5418 Bursts Detected with the Fermi Gamma-Ray Burst Monitor during its Most Prolific Activity. *Astrophys. J.* **749**, 122 (2012). [arXiv:1202.3157](#).
54. Oliphant, T. E. A Guide to NumPy. *Trelgol Publishing USA*, (2006).
55. Hunter, J. D. Matplotlib: A 2D graphics environment. *Comput. Sci. Eng.* **9**, 90–95 (2007).
56. Lyubarsky, Yu. A model for fast extragalactic radio bursts.. *Mon. Not. R. Astron. Soc.* **442**, L9–L13 (2014). [1401.6674](#).
57. Waxman, E. On the Origin of Fast Radio Bursts (FRBs). *Astrophys. J.* **842**, 34 (2017). [1703.06723](#).
58. Margalit, B. *et al.* Unveiling the engines of fast radio bursts, superluminous supernovae, and gamma-ray bursts. *Mon. Not. R. Astron. Soc.* **481**, 2407–2426 (2018). [1806.05690](#).
59. Sari, R., Piran, T. & Narayan, R Spectra and Light Curves of Gamma-Ray Burst Afterglows. *Astrophys. J.* **497**, L17–L20 (1998). [astro-ph/9712005](#).
60. Piran, T. Gamma-ray bursts and the fireball model. *Phys. Rep.* **314**, 575–667 (1999). [astro-ph/9810256](#).
61. Mészáros, P. Gamma-ray bursts. *Rep. Prog. Phys.*, 2259–2321 (2006). [astro-ph/0605208](#).
62. Kumar, P. & Zhang, B. The physics of gamma-ray bursts & relativistic jets. *Phys. Rep.* **561**, 1–109 (2015). [1410.0679](#).
63. Pe’er, A. & Zhang, B. Plasmas in Gamma-Ray Bursts: Particle Acceleration, Magnetic Fields, Radiative Processes and Environments. *Phys. Rep.* **7**, 33 (2019). [1902.02562](#).

64. Lyubarsky, Yu. Fast radio bursts from reconnection in magnetar magnetosphere. *arXiv e-prints*, arXiv:2001.02007 (2020). [2001.02007](#).
65. Bykov, A. *et al.* Particle Acceleration in Relativistic Outflows. *Space Sci. Rev.* **173**, 309–339 (2012). [1205.2208](#).
66. Blandford, R., Yuan, Y., Hoshino, M. & Sironi, L. Magnetoluminescence. *Space Sci. Rev.* **207**, 291–317 (2017). [1705.02021](#).
67. Lyutikov, M. Radio Emission from Magnetars. *Astrophys. J.* **580**, L65–L68 (2002). [astro-ph/0206439](#).
68. Lyutikov, M. Radius-to-frequency Mapping and FRB Frequency Drifts. *Astrophys. J.* **889**, 135 (2020). [1909.10409](#).

### Data Availability

The Konus-Wind data are from the corresponding authors on reasonable request.

### Code availability

Links to the Wind predicted ephemeris and clock accuracy are provided in the Methods section. XSPEC are freely available online.

### Acknowledgements

SP acknowledges support from the Program of development of M.V. Lomonosov Moscow State University (Leading Scientific School "Physics of stars, relativistic objects, and galaxies").

### Author contributions statement

Konus-Wind (KW) is a joint Russian-US gamma-ray burst experiment with the Russian gamma-spectrometer Konus on board the NASA *Wind* spacecraft. A.R., D.S., and D.F. performed the Konus-Wind data analysis. A.R., D.S., D.F., A.B. and S.P. contributed to the discussion of the results in the context of KW magnetar observations, magnetar emission models and FRB-magnetar connection. A.L. contributed to the KW

spectral analysis. S.G., A.T., and M.U. contributed to the KW data reduction. R.A., S.G., and D.F. contributed to the KW design and calibrations. R.A. was the principal investigator of the KW experiment and T.C. was the co-PI from the American side. A.R., D.S., and D.F. wrote the manuscript with the contributions of A.B. and S.P. All co-authors provided comments on the final version of the manuscript.

## **Additional information**

**Correspondence and requests for materials** should be addressed to [ridnaia@mail.ioffe.ru](mailto:ridnaia@mail.ioffe.ru).

## **Competing interests**

The authors declare no competing financial interests.

**Extended Data Table 1.** Temporal parameters: the burst start time relative to  $T_0$  (2nd column), the burst end time relative to  $T_0$  (3rd column), the total burst duration (4th column),  $T_{50}$  and  $T_{90}$  durations (5th and 6th columns, respectively) are given for specific energy band (1st column).

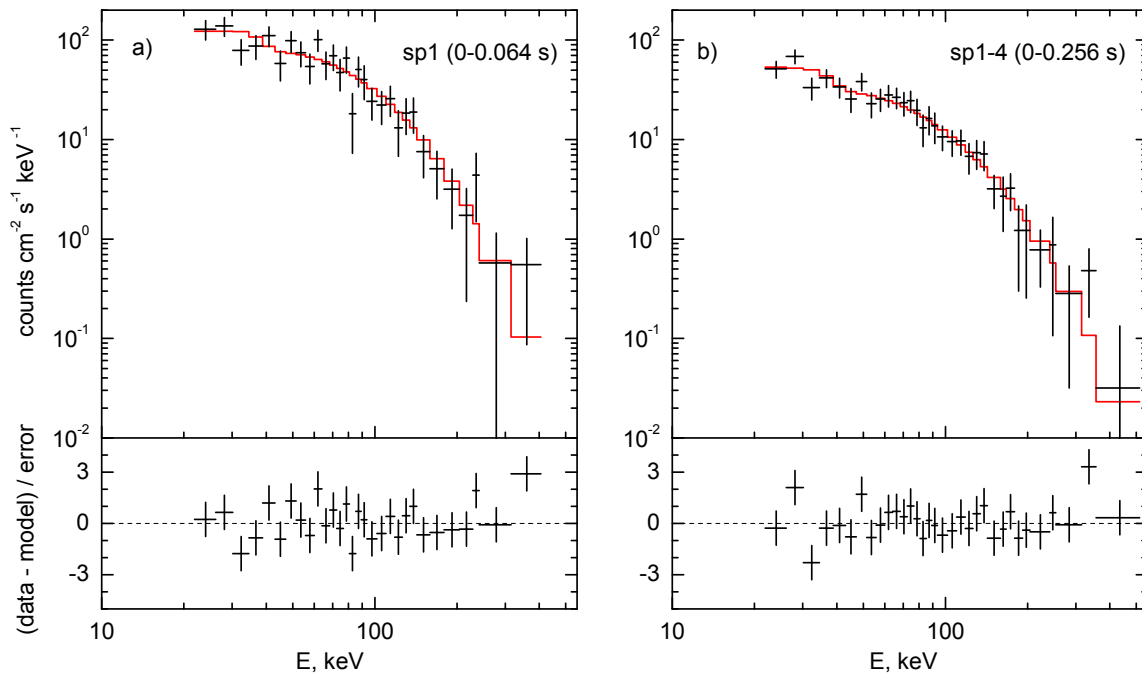
Band	$T_{\text{start}}$ (s)	$T_{\text{stop}}$ (s)	$T_{100}$ (s)	$T_{50}$ (s)	$T_{90}$ (s)
G1	-0.238	0.180	0.418	$0.078^{+0.010}_{-0.011}$	$0.326^{+0.032}_{-0.052}$
G2	-0.100	0.234	0.334	$0.074^{+0.021}_{-0.022}$	$0.238^{+0.053}_{-0.064}$
G1+G2	-0.220	0.264	0.484	$0.082^{+0.013}_{-0.009}$	$0.310^{+0.065}_{-0.034}$

**Extended Data Table 2.** Spectral fit results with thermal models (BB and 2BB) for two spectra: time-averaged spectrum (0.0–0.256 s) and the peak spectrum (0.0–0.064 s), measured near the peak count rate. The times are given relative to  $T_0$ . The errors are given at 90% CL. Model normalizations are proportional to the surface area  $R_{km}^2/d_{10}^2$ , where  $R_{km}$  is the source radius in km and  $d_{10}$  is the distance to the source in units of 10 kpc.

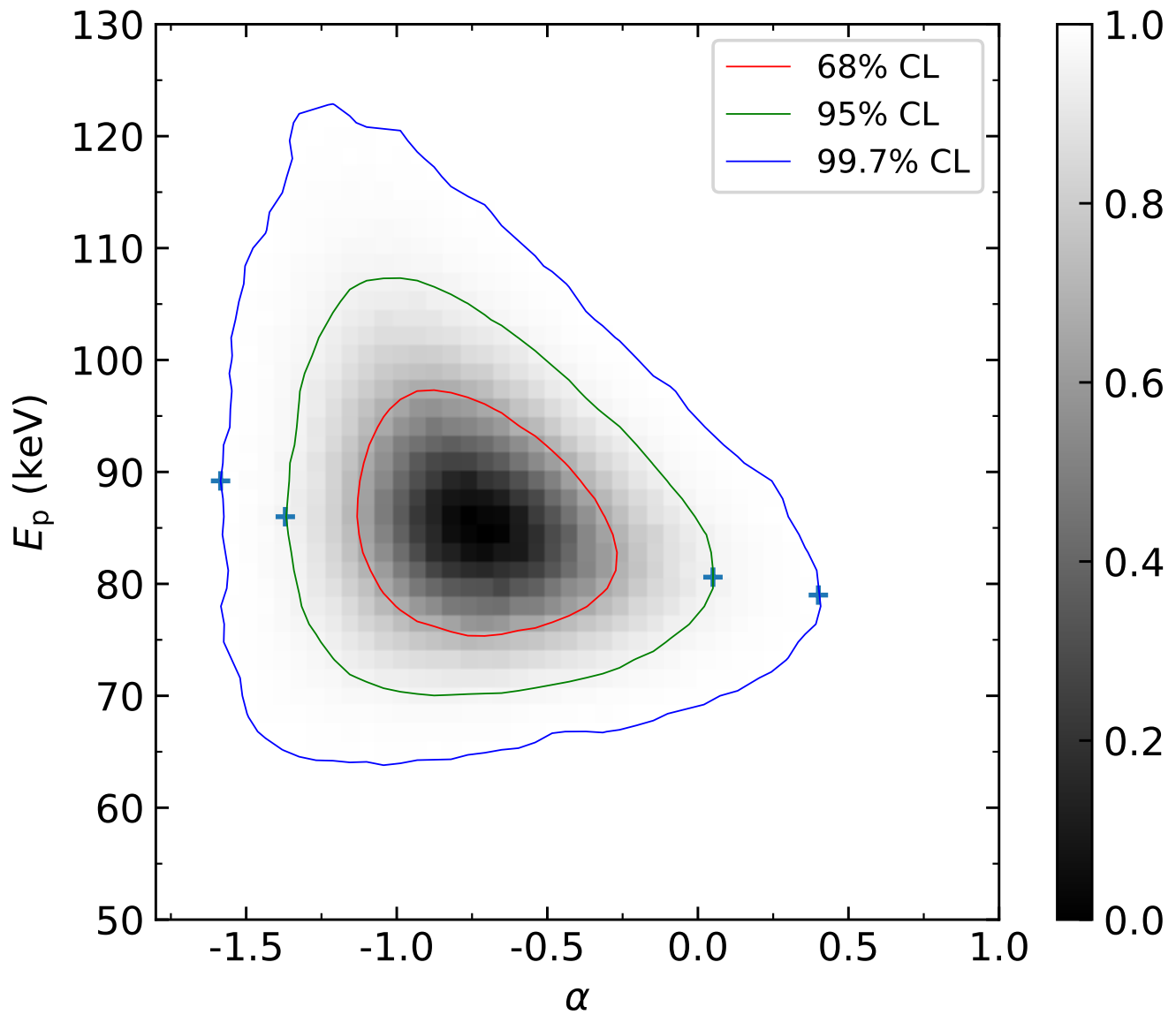
Interval (s)	Model	$kT_1$ (keV)	$\text{Norm}_1$ ( $R_{1,km}^2/d_{10}^2$ )	$kT_2$ (keV)	$\text{Norm}_2$ ( $R_{2,km}^2/d_{10}^2$ )	PG-stat / dof
0.0–0.064	BB	$19.5^{+1.7}_{-1.5}$	$3.6^{+1.3}_{-1.0}$	...	...	45.2 / 34
0.0–0.064	2BB	$13.6^{+3.4}_{-4.1}$	$9.3^{+13.6}_{-4.2}$	$35.4^{+21.8}_{-10.1}$	$0.16^{+0.94}_{-0.02}$	25.8 / 32
0.0–0.256	BB	$19.5^{+1.5}_{-1.4}$	$1.4^{+0.4}_{-0.3}$	...	...	82.6 / 48
0.0–0.256	2BB	$11.2^{+3.3}_{-3.8}$	$6.3^{+15.2}_{-3.2}$	$31.3^{+12.2}_{-6.7}$	$0.14^{+0.32}_{-0.11}$	49.1 / 46

**Extended Data Table 3.** Spectral fit results with non-thermal models (PL and CPL) for two spectra: time-averaged spectrum (0.0–0.256 s) and the peak spectrum (0.0–0.064 s), measured near the peak count rate. The times are given relative to  $T_0$ . The errors are given at 90% CL.

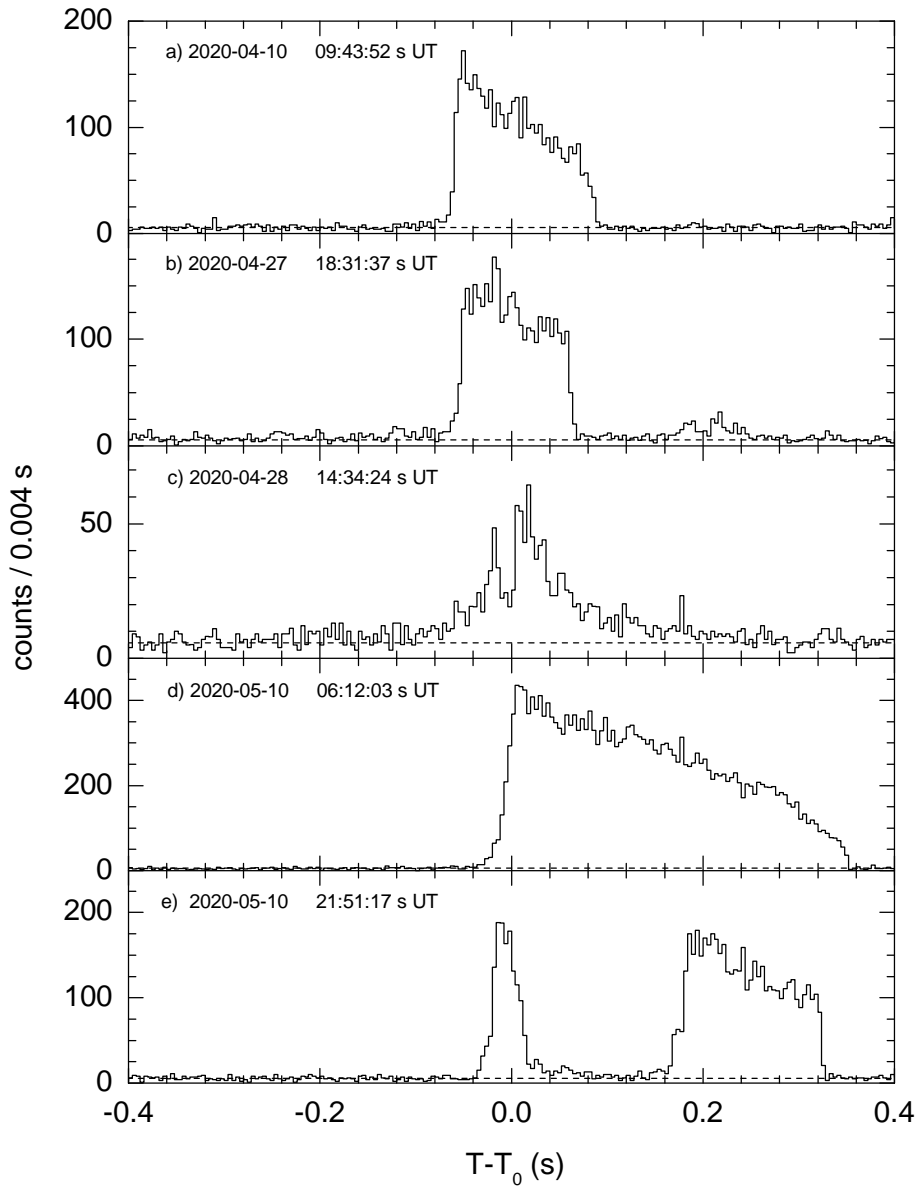
Interval (s)	Model	$\alpha$	$E_p$ (keV)	Flux (20–500 keV) $10^{-6} \text{ erg cm}^{-2} \text{ s}^{-1}$	PG-stat / dof
0.0–0.064	PL	$-2.02^{+0.12}_{-0.12}$	...	$6.7^{+0.9}_{-0.8}$	62.7 / 34
0.0–0.064	CPL	$-0.42^{+0.60}_{-0.58}$	$82^{+14}_{-10}$	$5.8^{+0.8}_{-0.6}$	25.4 / 33
0.0–0.256	PL	$-2.02^{+0.10}_{-0.09}$	...	$2.7^{+0.3}_{-0.3}$	85.8 / 48
0.0–0.256	CPL	$-0.72^{+0.47}_{-0.46}$	$85^{+15}_{-10}$	$2.4^{+0.3}_{-0.2}$	45.6 / 47



**Extended Data Figure 1.** *Konus-Wind* energy spectra of the April 28 event: (a) the spectrum containing peak count rate ( $T_0 - T_0 + 0.064$  s); (b) the time-integrated spectrum ( $T_0 - T_0 + 0.256$  s). The top panels present the count rates and their uncertainties (black points) and the best-fit CPL model (red line). The bottom panels show the fit residuals. Spectral channels are grouped for display purposes.



**Extended Data Figure 2.** Integrated probability of posterior marginal distribution for CPL model parameters  $\alpha$  and  $E_p$  (the time-integrated spectrum). The regions of the parameter space encompassing 68%, 95%, and 99.7% of the distribution probability are shown with contours. The symbols correspond to broadband flux density boundaries shown in Fig. 2.



**Extended Data Figure 3.** Time profiles of five short X-ray bursts from SGR 1935+2154 detected by *Konus-Wind* during the recent activation of the source in April-May 2020. The light curves shown here were recorded in the 18-320 keV energy band. Background count rates are indicated by horizontal dashed lines. In contrast with typical for magnetars, smooth time profiles of four other bursts, which start with a prominent, sharp rise of the intensity, the April 28 burst demonstrates slowly rising, spiky light curve.